ELSEVIER

Volume 184, Issue 6, June 2011

JOURNAL OF
SOLID STATE
CHEMISTRY

www.elsevier.com/locate/jssc

CONTENTS

Abstracted/indexed in BioEngineering Abstracts, Chemical Abstracts, Coal Abstracts, Current Contents/Physics, Chemical, & Earth Sciences, Engineering Index, Research Alert, SCISEARCH, Science Abstracts, and Science Citation Index. Also covered in the abstract and citation database SCOPUS®. Full text available on ScienceDirect®.

Regular Articles

Effect of ring coordination of pyridine-3,5-dicarboxylate and metatungstate to *Ln* ions on metatungstate structure: Synthesis, structure and optical property of four new compounds

Dan-Dan Liu, Ya-Guang Chen, Chun-Jing Zhang,
Hua-Xin Meng, Zhi-Chao Zhang and Chun-Xia Zhang

page 1355

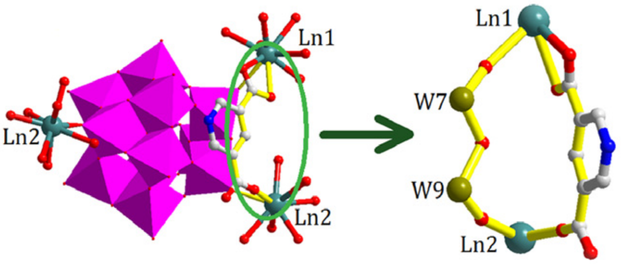

Four two-dimensional α-metatungstate and *Ln*-pyridine-3,5-dicarboxylate compounds have been synthesized. During the research, we elucidated the effect of ring coordination of pyridine-3,5-dicarboxylate on the structures of the POM-based hybrids.

Structure and magnetic properties of the cubic oxide fluoride $BaFeO_2F$

Frank J. Berry, Fiona C. Coomer, Cathryn Hancock,
Örn Helgason, Elaine A. Moore, Peter R. Slater,
Adrian J. Wright and Michael F. Thomas

page 1361

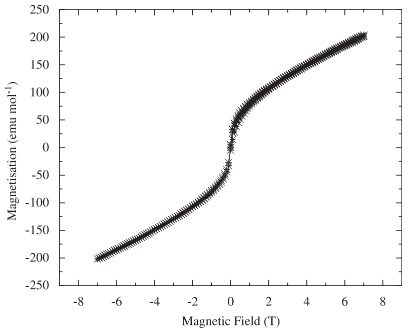

The cubic oxide fluoride of composition $BaFeO_2F$ has been synthesised and characterised.

Regular Articles—Continued

NMR relaxation study of the phase transitions and relaxation mechanisms of the alums $M\mathrm{Cr(SO_4)_2\cdot 12H_2O}$ (M = Rb and Cs) single crystals

Ae Ran Lim, Younkee Paik and Kye-Young Lim

page 1367

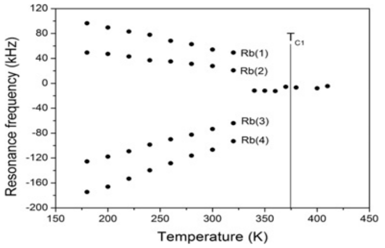

The physical properties and phase transition mechanisms of $M\mathrm{Cr(SO_4)_2\cdot 12H_2O}$ (M = Rb, Cs, and NH_4) single crystals have been investigated.

ZnO-based hollow microspheres with mesoporous shells: Polyoxometalate-assisted fabrication, growth mechanism and photocatalytic properties

Qiuyu Li, Weilin Chen, Mingliang Ju, Lin Liu and Enbo Wang

page 1373

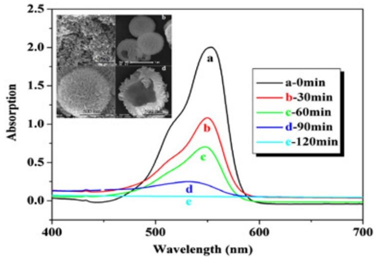

ZnO hollow spheres with mesporous shells were synthesized by an one-pot polyoxometalate-assisted solvothermal route. The ZnO hollow microspheres exhibited a high photocatalytic activity for decolorization of Rhodamine B (RhB) under UV irradiation.

Continued

Synthesis and crystal structure of two new cerium rhodium oxides: $Ce_{2/3-x}Rh_2^{3+}O_4$ ($x\sim0.12$) with Ce mixed valency and $Ce^{4+}Rh_2^{3+}O_5$

Hiroshi Mizoguchi, L.N. Zakharov, N.S.P. Bhuvanesh, A.W. Sleight and M.A. Subramanian

page 1381

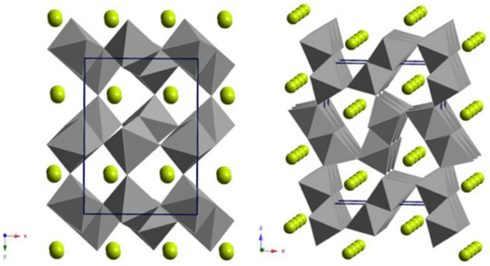

The new compounds $Ce_{2/3-x}Rh_2O_4$ ($x\sim0.11$–0.14) and $CeRh_2O_5$ have been prepared and their structures were determined from single crystal X-ray diffraction data. Electrical and magnetic properties were also evaluated.

New coordination polymers from 1D chain, 2D layer to 3D framework constructed from 1,2-phenylenediacetic acid and 1,3-bis(4-pyridyl)propane flexible ligands

Ling-Yun Xin, Guang-Zhen Liu and Li-Ya Wang

page 1387

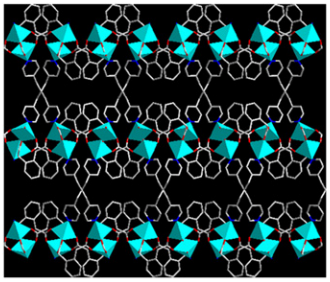

We show diverse supramolecular frameworks based on the same ligands (PHDA and BPP) and different metal acetate salts including 1D double-stranded chain, 2D → 2D twofold interpenetrated layer, and 3D self-penetration networks.

An *in situ* oxidation route to fabricate graphene nanoplate–metal oxide composites

Sheng Chen, Junwu Zhu and Xin Wang

page 1393

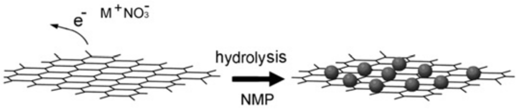

An improved soft chemical route to directly fabricate graphene nanoplate–metal oxide composites is reported from the *in situ* oxidation of graphene nanoplates.

Superior cycle performance of Sn@C/graphene nanocomposite as an anode material for lithium-ion batteries

Shuzhao Liang, Xuefeng Zhu, Peichao Lian, Weishen Yang and Haihui Wang

page 1400

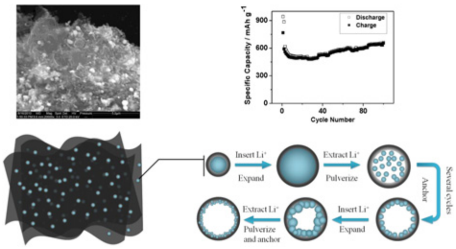

Tin nanoparticles coated with carbon embedded in graphene have been successfully fabricated by hydrothermal synthesis and subsequent annealing. This nanocomposite as an anode material for lithium-ion batteries exhibits superior cycle performance.

Structure and photoluminescence properties of Ce^{3+}-doped novel silicon-oxynitride $Ba_{4-z}M_zSi_8O_{20-3x}N_{2x}$ (M = Mg, Ca, Sr)

Y. Fang, Y.Q. Li, R.J. Xie, N. Hirosaki, T. Takade, X.Y. Li and T. Qiu

page 1405

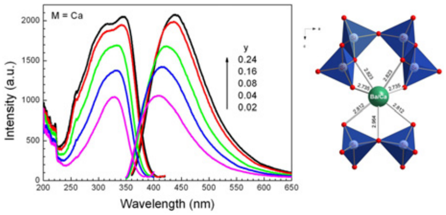

Excitation and emission spectra of $Ba_3MSi_8O_{18.5}N:Ce^{3+}$ (M = Ca, Ce^{3+} = 1 mol%) demonstrate that Ce^{3+}-doped novel silicon oxynitride emits blue light with a broad emission band in the range of 410–450 nm varying with the Ce^{3+} concentration under excitation at 330 nm. The luminescence properties are determined by the local crystal structure around Ba/Ca atom, where the activator ion of Ce^{3+} is occupied on the crystallographic site of Ba/Ca.

Mixed surfactants-directed the mesoporous silica materials with various morphologies and structures

Huiming Lin, Fengyu Qu, Xiang Wu, Ming Xue, Guangshan Zhu and Shilun Qiu

page 1415

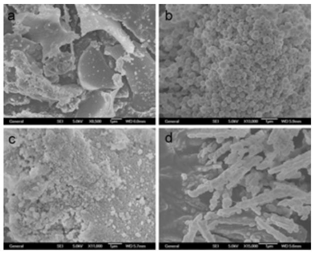

A new mixed surfactants system using alkyl carboxylic acids and PEPU as the co-template was used to synthesize mesoporous silica materials with various morphologies and structures.

Green synthesis of graphene nanosheets/ZnO composites and electrochemical properties

Jun Wang, Zan Gao, Zhanshuang Li, Bin Wang, Yanxia Yan, Qi Liu, Tom Mann, Milin Zhang and Zhaohua Jiang

page 1421

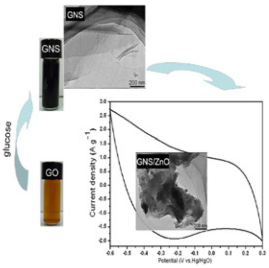

Glucose was used to synthesize GNS, then ZnO directly grew onto conducting graphene nanosheets as electrode materials for supercapacitor. Results showed that the composites have superior capacitive performance.

Heavy doping of H^- ion in $12CaO \cdot 7Al_2O_3$

Katsuro Hayashi

page 1428

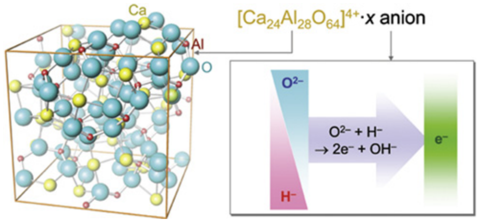

CaH_2 reduction markedly enhances H^- ion doping in $12CaO \cdot 7Al_2O_3$. The H^- ion incorporation is evaluated using optical absorption and ^1H-MAS-NMR spectra. Both H^- and O^{2-} ions are responsible for photogeneration of electrons.

Enhancement of photoelectric catalytic activity of TiO_2 film via Polyaniline hybridization

Yajun Wang, Jing Xu, Weizheng Zong and Yongfa Zhu

page 1433

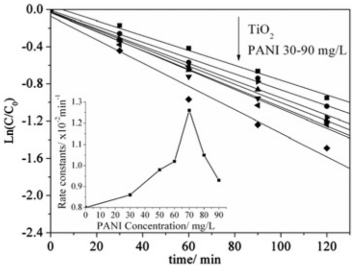

The effect of PANI content on 2,4-DCP degradation with initial concentration of 50 mg/L, external potential = 1.5 V. Inset: degradation rate constants of various PANI/TiO_2 films.

Neutron diffraction study of La_4LiAuO_8: Understanding Au^{3+} in an oxide environment

Joshua A. Kurzman, Stephanie L. Moffitt, Anna Llobet and Ram Seshadri

page 1439

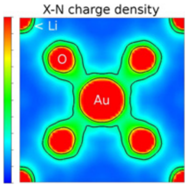

We report a neutron powder diffraction study of La_4LiAuO_8; this is the first neutron diffraction study of any stoichiometric oxide compound of gold. *X–N* maps, which make use of nuclear positions obtained from Rietveld refinement of time-of-flight neutron diffraction data and electron densities obtained from synchrotron X-ray powder diffraction data, point to the highly covalent nature of the Au–O bonding in La_4LiAuO_8. This is in good agreement with charge densities and Bader charges obtained from density functional relaxation of the structure.

$[R\text{-}C_7H_{16}N_2][V_2Te_2O_{10}]$ and $[S\text{-}C_7H_{16}N_2][V_2Te_2O_{10}]$; new polar templated vanadium tellurite enantiomers

Ethan C. Glor, Samuel M. Blau, Jeongho Yeon, Matthias Zeller, P. Shiv Halasyamani, Joshua Schrier and Alexander J. Norquist

page 1445

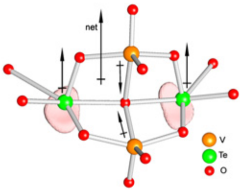

Two new vanadium tellurite enantiomers have been synthesized under mild hydrothermal conditions. Hydrogen-bonding between $[C_7H_{16}N_2]^{2+}$ cations and $[V_2Te_2O_{10}]_n^{2n-}$ layers results in polar structures that exhibit type 1 phase matching capabilities. Component and net dipole moments were calculated from atomic positions and iterative Hirshfeld partial charges.

Effect of lanthanide contraction on the mixed polyamine systems Ln/Sb/Se/(en + dien) and Ln/Sb/Se/(en + trien): Syntheses and characterizations of lanthanide complexes with a tetraelenidoantimonate ligand

Jing Zhao, Jingjing Liang, Yingli Pan, Yong Zhang and Dingxian Jia

page 1451

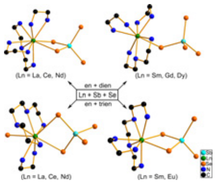

Two structural types of lanthanide(III) selenidoantimonates are formed in both en-dien and en-trien mixed polyamines across lanthanide series, indicating the lanthanide contraction effect on the structures of the lanthanide(III) selenidoantimonates.

Continued

Selective hydrothermal synthesis of BiOBr microflowers and Bi_2O_3 shuttles with concave surfaces

Peipei Xiao, Lingling Zhu, Yongchun Zhu and Yitai Qian

page 1459

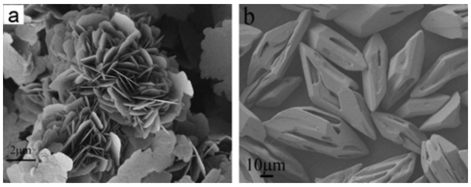

Through controlling the amount of NaOH added, BiOBr microflowers and Bi_2O_3 shuttles with concave surfaces were hydrothermally synthesized in the reaction system of $Bi(NO_3)_3$-hexadecyl trimethyl ammonium bromide (CTAB)–NaOH.

TiO_2/carbon nanotube hybrid nanostructures: Solvothermal synthesis and their visible light photocatalytic activity

Lihong Tian, Liqun Ye, Kejian Deng and Ling Zan

page 1465

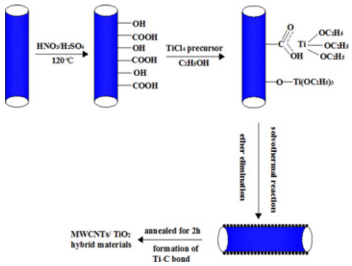

MWCNT/TiO_2 nanostructures have been prepared by solvothermal method, which exhibited higher visible-light-driven photocatalytic activity than that prepared by sol–gel method. The carbonaceous Ti–C bonds on the interface between TiO_2 and MWCNTs enhanced the photoabsorbance of the hybrid materials in the visible light region.

Two highly proton-conductive molecular hybrids based on ionized water clusters and poly-Keggin-anion chains

Mei-Lin Wei, Peng-Fei Zhuang, Qiu-Xiang Miao and Yan Wang

page 1472

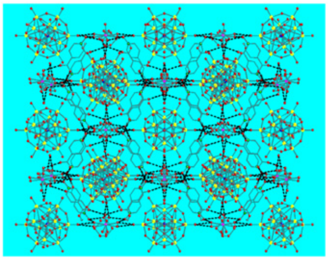

Two molecular hybrids constructed by ionized water clusters and poly-Keggin-anion chains showed high proton conductivities of 10^{-3} S cm^{-1} in the temperature range of 85–100 °C under 98% relative humidity.

Magnetic ordering of divalent europium in double perovskites $Eu_2\mathit{Ln}TaO_6$ (Ln = rare earths)

Magnetic interactions of Eu^{2+} ions determined by magnetic susceptibility, specific heat, and ^{151}Eu Mössbauer spectrum measurements

Yoshitaka Misawa, Yoshihiro Doi and Yukio Hinatsu

page 1478

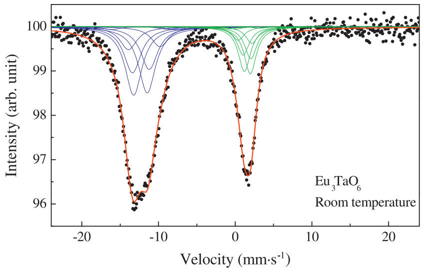

Magnetic properties of double perovskite-type oxides $Eu_2\mathit{Ln}TaO_6$ (Ln = Eu, Dy–Lu) were investigated. Magnetic susceptibility, specific heat, and ^{151}Eu Mössbauer spectrum measurements show that the Eu^{2+} ions at the 12-coordinate sites of the perovskite structure are antiferromagnetically ordered at ~4 K.

Probing the structure of complex solids using a distributed computing approach—Applications in zeolite science

Samuel A. French, Rosie Coates, Dewi W. Lewis and C. Richard A. Catlow

page 1484

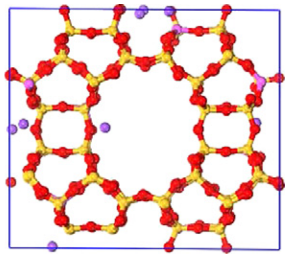

Aluminium distributions in zeolites are determined using e-science methods.

Synthesis of carbon-encapsulated iron nanoparticles via solid state reduction of iron oxide nanoparticles

M. Bystrzejewski

page 1492

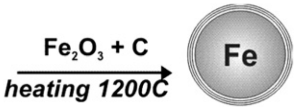

Reduction of iron oxide nanoparticles by carbon black at 1200 °C yields well crystallized carbon-encapsulated iron nanoparticles.

The $La_{0.95}Ni_{0.6}Fe_{0.4}O_3$–$CeO_2$ system: Phase equilibria, crystal structure of components and transport properties

Elena Konysheva and John T.S. Irvine

page 1499

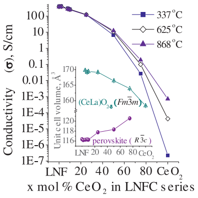

Diverse phase compositions and evolution of the crystal structure of components were observed in the (100−x) $La_{0.95}Ni_{0.6}Fe_{0.4}O_3$–$x$$CeO_2$ (LNFCx) system fabricated under oxidizing atmosphere. The presence of secondary phase(s) influences conductivity behavior in this system. A modified simple mixture model could explain conductivity of the LNFCx ($25 \leq x \leq 75$) compositions.

Elastic behavior of MFI-type zeolites: Compressibility of H-ZSM-5 in penetrating and non-penetrating media

Simona Quartieri, Gabriele Montagna, Rossella Arletti and Giovanna Vezzalini

page 1505

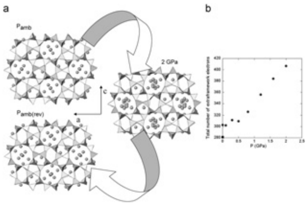

High-pressure behavior of H-ZSM-5 compressed in (16:3:1) methanol:ethanol:water: (a) projection of the structure along the [0 1 0] direction at P_{amb}, 2 GPa and after pressure release to original ambient conditions (P_{amb} (rev)), and (b) P-dependence of the extraframework content expressed as total number of electrons (gray square represents the number of the extraframework electrons at P_{amb} after decompression).

K_3*Ln*$[OB(OH)_2]_2[HOPO_3]_2$ (*Ln* = Yb, Lu): Layered rare-earth dihydrogen borate monohydrogen phosphates

Yan Zhou, Stefan Hoffmann, Ya-Xi Huang, Yurii Prots, Walter Schnelle, Prashanth W. Menezes, Wilder Carrillo-Cabrera, Jörg Sichelschmidt, Jin-Xiao Mi and Rüdiger Kniep

page 1517

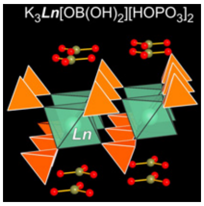

Two isotypic layered rare-earth borate phosphates, K_3*Ln*$[OB(OH)_2]_2[HOPO_3]_2$ (*Ln* = Yb, Lu), were synthesized hydrothermally and the crystal structures were determined by single-crystal X-ray diffraction. The structure can be described by stacking of Glaserite-type slabs and dihydrogen borate layers separated by potassium cations.

Infrared absorptive properties of Al-doped ZnO divided powder

H. Serier, A. Demourgues, J. Majimel and M. Gaudon

page 1523

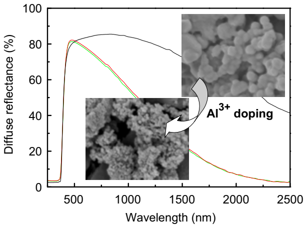

Al-doped ZnO powders synthesised from Pechini routes after annealing under argon at low temperatures exhibit high optical selectivity: large Infrared absorption/high visible transparency.

Structural and magnetic properties of nanoclusters in GaMnAs granular layers

K. Lawniczak-Jablonska, J. Bak-Misiuk, E. Dynowska, P. Romanowski, J.Z. Domagala, J. Libera, A. Wolska, M.T. Klepka, P. Dluzewski, J. Sadowski, A. Barcz, D. Wasik, A. Twardowski and A. Kwiatkowski

page 1530

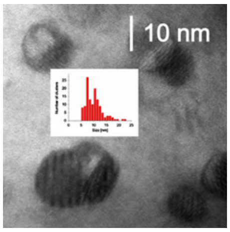

After thermal processing of GaMnAs layers the clear evidence of formation of clusters with two structures is provided, which scales with the Mn magnetic moment. The structure of clusters cannot be a priori assumed as it is commonly done.

Preparation of blue-emitting $CaMgSi_2O_6:Eu^{2+}$ phosphors in reverse micellar system and their application to transparent emissive display devices

Sungho Choi, Se-Won Tae, Jung-Hyun Seo and Ha-Kyun Jung

page 1540

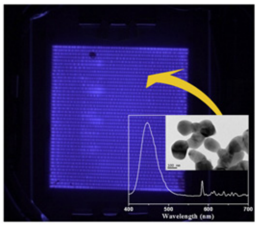

Blue-emitting $CaMgSi_2O_6:Eu^{2+}$ nanophosphors coated transparent luminescent layers can be obtained. It illuminates the characteristic blue emission, spectrum centered at 425 nm wavelength, under the Ne–Xe mixed gas plasma discharge condition.

Continued

Synthesis and characterization of monodisperse, mesoporous, and magnetic sub-micron particles doped with a near-infrared fluorescent dye

Xavier Le Guével, Robert Nooney, Colette McDonagh and Brian D. MacCraith

page 1545

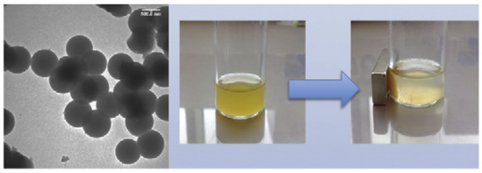

Hydrophobic fluorescent Ruthenium complex has been loaded into the mesopores as a surrogate drug to simulate drug delivery and to enhance the multifunctionality of the magnetic NIR emitting particles.

Enhanced thermal- and photo-stability of acid yellow 17 by incorporation into layered double hydroxides

Qian Wang, Yongjun Feng, Junting Feng and Dianqing Li

page 1551

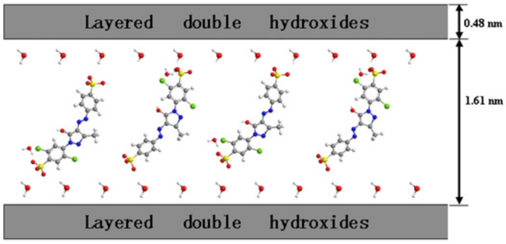

Acid yellow anions were successfully assembled into ZnAl layered double hydroxides (LDH) to produce a novel organic–inorganic composite pigment by a simple method involving separate nucleation and aging steps (SNAS).

An approach to preparing porous and hollow metal phosphides with higher hydrodesulfurization activity

Limin Song, Shujuan Zhang and Qingwu Wei

page 1556

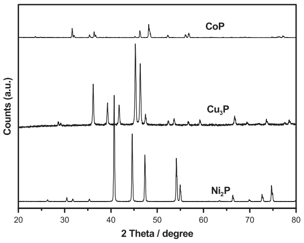

Bulk and supported Ni_2P, Cu_3P, and CoP were prepared by thermal treatment of their metal and amorphous red phosphorus mixtures. Porous and hollow Ni_2P particles were successfully synthesized by this method also. In the experimental condition, a Ni_2P/SiO_2 catalyst exhibits excellent hydrodesulfurization activity for dibenzothiophene.

Ca-intercalated graphite as a hydrogen storage material: Stability against decomposition into CaH_2 and graphite

C.R. Wood, N.T. Skipper and M.J. Gillan

page 1561

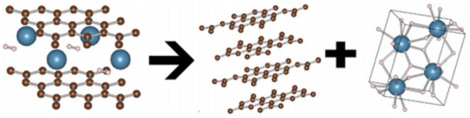

The hydrogenation of Ca–graphite (left) results in its decomposition into pure graphite (middle) and CaH_2 (right).

A re-investigation of the crystal structure and luminescence of $BaCa_2MgSi_2O_8$:Eu^{2+}

Cheol-Hee Park, Tae-Hoon Kim, Yoshinori Yonesaki and Nobuhiro Kumada

page 1566

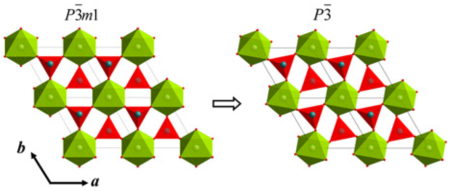

A combined powder X-ray and neutron Rietveld method reveals that $BaCa_2MgSi_2O_8$ crystallizes in the trigonal space group $P\bar{3}$, instead of the previously believed space group $P\bar{3}m1$ from X-ray diffraction data.

Rapid Communications

Preparation and drug release behavior of temperature-responsive mesoporous carbons

Xiufang Wang, Ping Liu and Yong Tian

page 1571

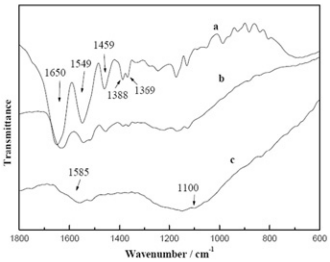

The bands located at 1650 and 1549 cm^{-1} could be assigned to C=O stretching and N–H bending vibrations for polymer PNIPAAm (a). The bands at 1388 and 1369 cm^{-1} were due to isopropyl group, and the band at 1459 cm^{-1} was related to the bending vibration of C–H (a). For the PNIPAAm/OMCs composite, the characteristic bands of polymer were still observed besides those for carbon materials and the bands at around 1585 cm^{-1} and a broad band at about 1100 cm^{-1} were characteristics for the carbon materials(c). In addition, little shifts of C=O and N–H bands compared to the pure PNIPAAm were also observed (b), indicating a weak interaction between the polymer and carbon material. These results could be a proof that the PNIPAAm has been incorporated into the carbon material.

Crystal structure of $Bi_{1-x}Tb_xFeO_3$ from high-resolution neutron diffraction

Stefan Saxin and Christopher S. Knee

page 1576

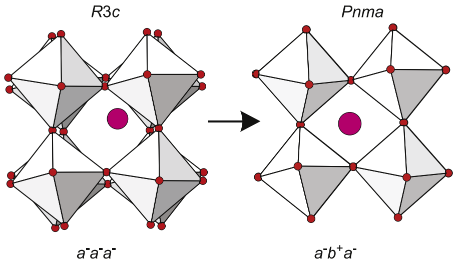

High resolution neutron powder diffraction has been used to study the evolution of the RT crystal structure of $Bi_{1-x}Tb_xFeO_3$ ($0.05 \leq x \leq 0.25$) with terbium content. A transition from polar *R*3*c* to centrosymmetric *Pnma* symmetry is observed. The antiferromagnetic ordering temperature and size of the ordered magnetic moment are relatively insensitive to the change of crystal structure.

Author inquiries

For inquiries relating to the submission of articles (including electronic submission where available) please visit this journal's homepage at http://www.elsevier.com/locate/jssc. You can track accepted articles at http://www.elsevier.com/trackarticle and set up e-mail alerts to inform you of when an article's status has changed. Also accessible from here is information on copyright, frequently asked questions and more.
Contact details for questions arising after acceptance of an article, especially those relating to proofs, will be provided by the publisher.

Language services. Authors who require information about language editing and copyediting services pre- and post-submission please visit http://www.elsevier.com/locate/languagepolishing or our customer support site at http://epsupport.elsevier.com. Please note Elsevier neither endorses nor takes responsibility for any products, goods or services offered by outside vendors through our services or in any advertising. For more information please refer to our Terms & Conditions http://www.elsevier.com/termsandconditions

For a full and complete Guide for Authors, please go to: http://www.elsevier.com/locate/jssc

Journal of Solid State Chemistry has no page charges.